White Rose Research Online

eprints@whiterose.ac.uk
https://eprints.whiterose.ac.uk
Universities of Leeds, Sheffield and York

Deposited via The University of Leeds.

White Rose Research Online URL for this paper:
https://eprints.whiterose.ac.uk/id/eprint/247217/

Version: Accepted Version

Article:
Li, L., Kumar, S., Moorhouse, T. et al. (Accepted: 2026) Transient epitaxial dynamics and cascade continuity in long-duration terahertz quantum cascade laser growth. Journel of Applied Physics. ISSN: 0021-8979 (In Press)

This is an author produced version of an article accepted for publication in Journal of Applied Physics, made available via the University of Leeds Research Outputs Policy under the terms of the Creative Commons Attribution License (CC-BY), which permits unrestricted use, distribution and reproduction in any medium, provided the original work is properly cited.

Reuse
This article is distributed under the terms of the Creative Commons Attribution (CC BY) licence. This licence allows you to distribute, remix, tweak, and build upon the work, even commercially, as long as you credit the authors for the original work. More information and the full terms of the licence here:
https://creativecommons.org/licenses/

Takedown
If you consider content in White Rose Research Online to be in breach of UK law, please notify us by emailing eprints@whiterose.ac.uk including the URL of the record and the reason for the withdrawal request.

UNIVERSITY OF LEEDS
University of Sheffield
UNIVERSITY of York

Transient epitaxial dynamics and cascade continuity in long-duration terahertz quantum cascade laser growth

Lianhe Li[1*], Sumona Kumar[1], Thomas Moorhouse[1], Minghui You[2], A. Giles Davies[1], Edmund H. Linfield[1]

[1] School of Electronic and Electrical Engineering, University of Leeds, Woodhouse Lane, Leeds LS2 9JT, UK

[2] College of Engineering and Technology, Changchun Normal University, No. 677 Changji beixian, Changchun City, Jilin Province, P.R. China, post code 130032

[*] Email: l.h.li@leeds.ac.uk

Abstract

Reproducibility in terahertz-frequency quantum cascade laser (THz QCL) growth by molecular beam epitaxy is commonly discussed in terms of controlling growth parameters, including growth rate, alloy composition, and doping level. Although control of these parameters is essential, the role of long-term dynamical stability in preserving the structural continuity of the cascade remains less well understood. Here, we provide experimental support for a physical picture in which discrete transient growth events can partition the active region into portions with different effective periodicities, thereby disrupting cascade continuity in a manner distinct from monotonic drift. Using in-situ pyrometry phase analysis combined with high-resolution x-ray diffraction (HRXRD) and device characterization, we show that nominally identical GaAs/AlGaAs THz QCL structures can exhibit markedly different dynamical evolution during growth. These differences are reflected in pyrometry phase departure, satellite peak splitting, and device behavior consistent with a narrowed common transport window. Representative post-operation images of Ga-source components show liquid-Ga accumulation and morphologies consistent with redistribution near the evaporation aperture after extended operation. These observations, together with the pyrometry and HRXRD results, are consistent with a possible Ga-source contribution to transient growth instability during long-duration MBE growth. The work also highlights the sensitivity of THz QCL structures as probes of transient epitaxial dynamics.

1. Introduction

Terahertz (THz) frequency radiation has attracted extensive attention because of its potential applications in spectroscopy, imaging, sensing, security screening, and high-speed wireless communications [1,2]. Since the first demonstration of the terahertz quantum cascade laser (THz QCL) [3], substantial progress has been achieved in extending the operating frequency range [2, 4-5], improving output power [6–8], and increasing the maximum operating temperature [9 – 11]. In particular, GaAs/AlGaAs THz QCLs have emerged as one of the most mature semiconductor platforms for coherent THz generation.

The operation of THz QCLs relies critically on precisely engineered intersubband transitions within a complex multilayer heterostructure. This requires accurate control of individual layer thicknesses and alloy compositions with sub-nanometer precision over a total active-region thickness up to 24 μm [7, 12-15]. Even relatively small deviations in growth conditions can modify subband alignment, carrier transport, and optical gain, thereby strongly affecting device performance [9–11].

Despite major advances in molecular beam epitaxy (MBE) growth techniques, it remains a significant challenge to achieve highly reproducible growth of THz QCLs, particularly across different growth campaigns and MBE systems [12–15]. Previous studies have established that THz QCL active regions place exceptionally stringent demands on growth rate calibration, thickness control, alloy composition accuracy, interface quality, flux stability, and run-to-run reproducibility [12–15]. Real-time monitoring

techniques such as pyrometric spectrometry have also been shown to provide a powerful means of calibrating growth rates, monitoring QCL growth evolution, and compensating long-term growth rate drift during epitaxy [7, 15, 16].

Within this established framework, structural and performance variations are commonly interpreted in terms of average structural descriptors and long-term monotonic trends, including superlattice period, alloy composition, and growth-rate drift. Previous studies have also shown that long-duration THz QCL growth can exhibit both continuous and discrete instabilities. HRXRD measurements have documented high-order satellite broadening, multiple satellite features, and peak splitting associated with Ga growth-rate fluctuations or discrete Ga-flux shifts [13–14]. In one reported case, a THz QCL grown with a Ga cell that later failed showed split superlattice reflections. The corresponding superlattice periods differed from the design by approximately 1.1% and 3.6% [14]. The same study associated smoother high-order broadening with a continuous Ga-flux drift of approximately 1% during active-region growth [14]. These studies showed that high-order HRXRD satellites are sensitive to growth instability. However, the temporal evolution and consequences of such transient instabilities during long-duration growth remain less well understood. Their physical origins also remain uncertain.

THz QCL active regions can contain tens to several hundred cascade periods and require extended growth durations [3]. Their repeated multilayer structure makes them particularly sensitive to transient changes during growth. A discrete event that alters the growth state over a finite interval can leave a persistent structural signature across a substantial fraction of the completed active region. The effects of such perturbations can be retained as changes in effective periodicity, producing measurable HRXRD signatures and potentially modifying carrier transport by disrupting cascade continuity. Here, cascade continuity refers to structural consistency from one cascade period to the next throughout the active region. A discrete change in effective periodicity therefore represents a break in this continuity. This sensitivity makes THz QCL structures useful probes of the relationship between long-duration growth dynamics, retained structural signatures, and device behavior.

In this work, we investigate long-duration growth dynamics in nominally identical THz QCL structures using in-situ pyrometry, HRXRD, and device characterization. Together, these measurements support a physical picture in which the effects of discrete transient growth events are retained as changes in effective periodicity, with associated consequences for cascade continuity and device transport. Post-operation observations of Ga-source morphology are presented separately as supporting evidence for a possible Ga-source contribution to the transient behavior.

2. Experimental details

The GaAs/AlGaAs THz QCL heterostructures investigated in this work were grown by solid-source molecular beam epitaxy (MBE) on semi-insulating GaAs substrates. The two principal samples, L1905 and L1907, have nominally identical 10-μm-thick active regions based on the same established design. The use of this established design provides a fixed structural basis for examining differences associated with their respective growth histories. Each active region contains approximately 81 cascade periods of the 3.4-THz bound-to-continuum (BTC) sub-stack reported in Ref. [5] and has an Al barrier composition of approximately 18%. They were grown consecutively using the same programmed layer sequence, nominal doping profile, and substrate-temperature setpoint under otherwise nominally identical growth conditions. A separate pair of samples based on the BTC design of Ref. [17] was also grown with the same nominal design but different numbers of periods. The resulting active-region thicknesses were approximately 12 and 24 μm. The two samples were grown at different times under nominally identical conditions, using the same pre-growth calibration and growth-rate-compensation procedures. They were used to compare epitaxial evolution over different total growth durations. In addition, we examined a reference structure comprising a 40-nm AlAs layer followed by approximately 15 μm of undoped GaAs. This type of structure is routinely used for background-doping assessment; here, it was used to assess

long-duration growth stability outside the repeated QCL active-region architecture. The QCL samples followed a standard single-plasmon waveguide configuration. The complete heterostructure comprised a GaAs buffer layer, an AlGaAs etch-stop layer, an n+-doped GaAs bottom contact layer, the THz QCL active region, and a heavily n++-doped GaAs top contact layer. All samples were grown using identically specified 85-cc Ga cells with an insert.

Immediately prior to growth, the GaAs and AlAs growth rates were calibrated using in-situ pyrometric spectrometry (kSA BandiT), which enables real-time monitoring of interference oscillations during epitaxy [15, 16]. This approach has previously been shown to achieve a thickness accuracy of approximately 0.5% for a 24-μm-thick THz QCL growth [7]. Pyrometry oscillations were also recorded continuously throughout the QCL active-region growth for post-growth phase-evolution analysis.

Post-growth structural characterization was carried out by high-resolution x-ray diffraction (HRXRD) ω–2θ scanning around the symmetric GaAs (004) reflection using a Jordan Valley QC3 diffractometer with Cu Kα1 radiation (λ = 1.54056 Å). The cascade period length of the QCLs was determined from the angular positions and order separation of satellite peaks [18]. High-order satellite reflections were examined in particular because these features are highly sensitive to cumulative thickness variations and long-range structural coherence across the entire active region.

The QCL wafers were processed into single-plasmon ridge-waveguide structures using standard photolithography and wet chemical etching techniques, and the substrate was thinned to ∼180 μm. Top and bottom electrical contacts were formed using Ti/Au and AuGeNi metallization, respectively. The processed devices were cleaved into Fabry–Pérot cavities and indium-soldered onto copper submounts. Pulsed electrical and optical measurements were performed in a cryocooler system using 1 μs pulses at a repetition frequency of 10 kHz, corresponding to a duty cycle of 1%. The terahertz output power emitted from a single facet was measured using an absolute terahertz power meter (Thomas Keating) positioned directly outside the cryocooler window, without a light pipe or Winston cone. No correction was applied for the optical collection efficiency. The maximum operating temperature, T_{max}, was defined as the highest heat-sink temperature at which lasing emission remained detectable under the specified pulsed measurement conditions.

3. Structural characterization by HRXRD

Fig. 1 shows the HRXRD ω–2θ scans of L1905, L1907, and a representative intentionally heterogeneous active-region structure (Stack). The scans are plotted on a logarithmic intensity scale to show the full dynamic range of the satellite peak structure. The Stack trace was measured from a previously reported broadband heterogeneous THz QCL structure [5]. In this structure, active-region sections with different design periodicities were deliberately combined. The trace is included here as a reciprocal-space reference for an intentionally introduced periodicity discontinuity. Both L1905 and L1907 exhibit well-resolved satellite peaks extending to high diffraction orders, showing that the intended superlattice periodicity is retained overall in both structures. However, their high-order satellite features differ markedly: L1907 shows sharp, regularly spaced satellite peaks, whereas L1905 exhibits pronounced broadening and splitting at high diffraction orders. In contrast, the Stack trace shows strongly suppressed and irregular high-order satellite peaks, reflecting destructive interference between diffraction contributions from the deliberately combined sub-stacks with different periodicities.

The satellite peak full-width at half maximum (FWHM) values extracted from single-Gaussian fitting are plotted as a function of diffraction order in the right inset of Fig. 1(a). For L1907, the FWHM remains narrow and increases only weakly with order, consistent with a single-Gaussian description throughout. Applying the phenomenological broadening model [10, 14]

$$w^2 = w_0^2 + (2.36\sigma\omega)^2,$$

where w is the measured FWHM of a satellite peak, w_0 is an order-independent contribution associated with instrumental broadening and finite stack thickness, ω is the angular separation of the satellite from the zeroth-order reflection, and σ is the standard deviation of the fractional superlattice-period variation, yields an effective period fluctuation of $\sigma \approx 0.085\%$, indicating excellent long-range thickness uniformity. This value is comparable to the period uniformity reported for high-performance GaAs/AlGaAs THz QCL structures grown under optimized conditions [10].

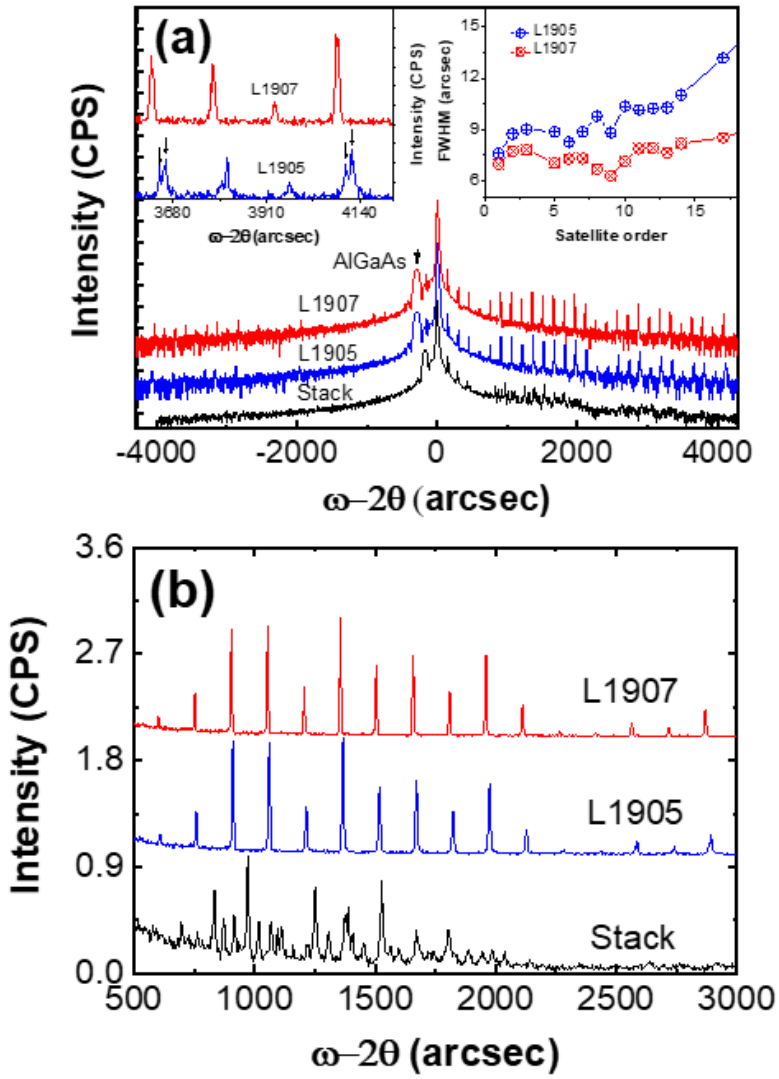


Fig. 1. (a) HRXRD ω–2θ scans of L1905, L1907, and the heterogeneous Stack structure on a logarithmic intensity scale, vertically offset for clarity. The arrow marks the AlGaAs etch-stop feature. Left inset: high-angle satellite region for L1905 and L1907 on a linear scale. Right inset: satellite-peak FWHM from single-Gaussian fits versus diffraction order; values for the split high-order L1905 features are apparent linewidths. (b) Satellite region (500–3000 arcsec) on a linear scale, showing sharp, regularly spaced peaks for L1907, broadened and split features for L1905, and suppressed, irregular peaks for Stack.

L1905 presents a markedly different diffraction signature. Its high-order satellite features become substantially broader and ultimately split into resolved components, with the apparent FWHM reaching approximately 13 arcsec at order 17, compared with approximately 8 arcsec for L1907. These FWHM values were obtained by fitting the overall split feature with a single Gaussian. They are therefore used only as apparent linewidths that characterize the loss of reciprocal-space coherence, rather than as true single-peak broadening parameters. The resolved splitting is clearly visible in the left inset to Fig. 1(a), indicating the presence of at least two effective-periodicity contributions within the active region. As an example, multi-component Gaussian analysis of the +21 and +22 satellites is provided in the Supplementary Material to quantify the resolved high-order splitting. Analysis of the resolved satellite components yields effective superlattice periods of approximately 124.58 and 125.03 nm, separated by

approximately 0.45 nm, corresponding to a relative difference of about 0.36%. Although these components establish multiple effective-periodicity contributions within the grown structure, they cannot be assigned uniquely to specific depth intervals or temporal stages of the growth.

The distinction between broadening and splitting is important. Conventional interface roughness introduces largely uncorrelated local fluctuations and is expected to produce symmetric broadening or diffuse scattering, rather than resolvable splitting of high-order satellite peaks. By contrast, the split satellite structure observed in L1905 indicates a correlated modulation of the effective superlattice period extending over substantial portions of the active region. Higher-order satellite peaks are particularly sensitive to this type of extended modulation because even small variations in the effective period produce increasingly resolvable differences at larger diffraction orders.

This observation is consistent with previous reports on GaAs/AlGaAs THz QCL structures, where high-order satellite splitting was attributed to discrete Ga-flux shifts during growth [13–14]. At this stage, HRXRD therefore establishes the retained structural signature—multiple effective-periodicity contributions and reduced long-range reciprocal-space coherence—while the dynamical origin of this modulation is examined in Section 4.

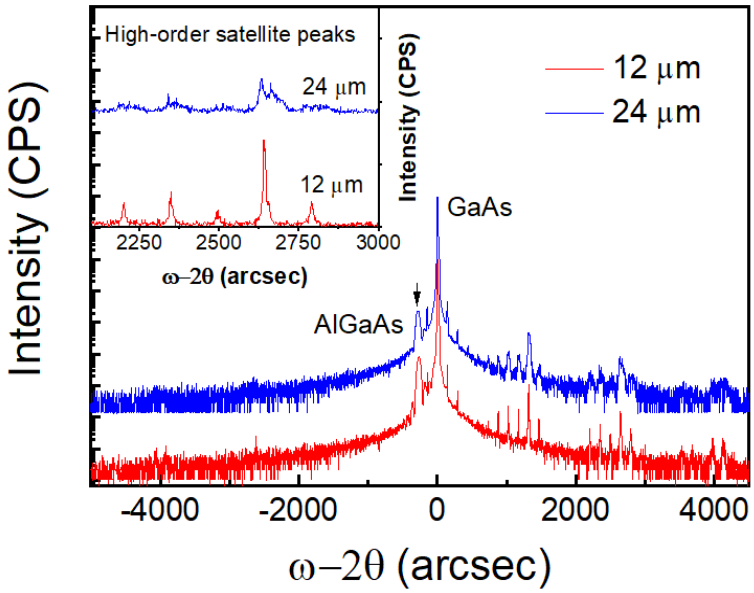


Fig. 2. HRXRD ω–2θ scans of two GaAs/AlGaAs THz QCLs with the same nominal active-region design and thicknesses of approximately 12 and 24 μm. The scans are plotted on a logarithmic intensity scale and vertically offset for clarity. The arrow marks the AlGaAs etch-stop feature. Inset: high-order satellite region on a linear scale.

Fig. 2 compares HRXRD ω–2θ scans of two GaAs/AlGaAs THz QCLs with the same nominal active-region design but different thicknesses of approximately 12 μm and 24 μm. The thinner structure retains well-resolved high-order satellite peaks, whereas the thicker structure exhibits substantially broader and partially merged satellite features with reduced high-order peak intensity. Such broadening can contain contributions from several sources, including local interface disorder, monotonic growth-rate drift, and longer-range correlated variations arising from transient or discrete growth perturbations.

Monotonic growth-rate drift associated with source depletion is mitigated in these long-duration growths using the compensation procedure described previously [15]. Indeed, a separate growth-rate-compensated 12/24-μm THz QCL pair based on a different active-region design retained well-resolved high-order satellite features in both structures, as shown in the Supplementary Material. This shows that extended growth duration under growth-rate-compensated conditions does not necessarily lead to pronounced high-order satellite broadening. At the same time, a longer growth duration provides a larger temporal window and therefore a greater opportunity for discrete transient perturbations to occur. If such an event alters the effective growth conditions over a finite interval, its structural consequences can persist

over many subsequent cascade periods. This can produce a correlated modulation of the effective periodicity and a corresponding loss of high-order diffraction coherence. The following section therefore examines the in-situ growth dynamics associated with this possibility.

4. In-situ evidence of transient growth dynamics and source morphology

The temporal stability of the epitaxial process was further examined using in-situ pyrometry oscillations [15, 16]. The analysis focused on the phase evolution of the oscillatory signal relative to a constant-rate reference trajectory, rather than only on the average growth rate. This relative phase evolution provides a sensitive measure of the long-term phase stability of the growth process. Details of the signal processing, transfer-matrix reference calculation, piecewise effective-growth-rate estimation, and sensitivity analysis are provided in Supplementary Section S1.

The phase departure was quantified from the temporal displacement of pyrometry oscillations relative to a constant-growth-rate reference trajectory. For growth at a constant rate, experimental and calculated oscillations should maintain a stable phase relationship. Within the effective-growth-rate representation used here, and with the optical parameters held fixed, the phase departure from this reference is, to first order, proportional to the time integral of the relative growth-rate variation,

$$\Delta\phi(t) \propto \int_0^t \frac{\Delta G(t')}{G_0} dt'$$

where G_0 is the reference growth rate and $\Delta G(t')$ represents the time-dependent deviation from this reference. In the present growths, the effect of gradual source-depletion-driven growth-rate drift is mitigated by the established growth-rate-compensation procedure [15]. The phase evolution is therefore particularly useful for identifying departures from this compensated long-term behavior. A discrete transient event can shift the epitaxial process from one effective growth-rate state to another, changing the rate of phase accumulation relative to the reference trajectory. If the new state persists, the phase departure continues to evolve with a slope determined by that state until another transition occurs. Because growth time can be related approximately to accumulated thickness, the phase record provides temporal information that can be mapped approximately onto depth within the active region. By contrast, post-growth structural measurements such as HRXRD characterize the completed structure and can reveal multiple retained periodicities, but do not, by themselves, establish when during growth a given perturbation occurred. Phase analysis therefore complements the endpoint information obtained from post-growth measurements.

Fig. 3 compares the phase evolution of L1905 and L1907 relative to their constant-growth-rate references. As shown in Fig. 3(a), L1907 maintains a relatively stable phase throughout the deposition, suggesting that its effective growth rate remains close to the compensated growth rate. In contrast, L1905 exhibits a clear change in phase evolution during deposition. A systematic phase lag becomes pronounced after approximately 5–6 h, with the accumulated phase departure reaching approximately 0.6-rad by the end of growth. Because the experimental and reference trajectories are aligned to a common phase origin, the 0.6-rad value represents the phase mismatch accumulated relative to that origin and does not by itself quantify the underlying change in growth behavior. This phase-evolution behavior is not described by a simple monotonic drift and is instead consistent with a transition between effective growth-rate states.

To quantify the associated change in effective growth rate, the L1905 pyrometry record was analyzed using the piecewise procedure described in Supplementary Section S1. The analysis gives best-matched interval-averaged effective growth rates of approximately 0.8372 and 0.8345 μm h^{-1} for two successive comparison intervals, differing by approximately 0.32%. The approximately 0.32% difference is close to the 0.36% effective-period difference obtained independently by HRXRD. Together, the two measurements are consistent with a transition between effective growth-rate states during active-region growth, with the associated structural signature retained as multiple effective periodicities in the

completed structure. However, this numerical similarity alone does not establish a one-to-one correspondence between the pyrometry intervals and the resolved HRXRD components.

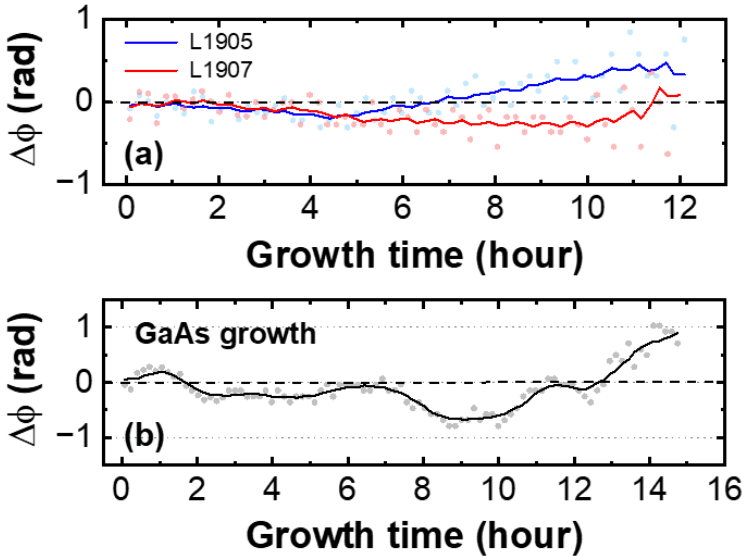


Fig. 3. Phase departure estimated from the temporal displacement of pyrometry extrema relative to a constant-growth-rate reference matched to the early stable portion of each growth: (a) L1905 and L1907; (b) thick-GaAs reference. Solid lines are LOWESS-smoothed guides to the eye and were not used in the quantitative analysis.

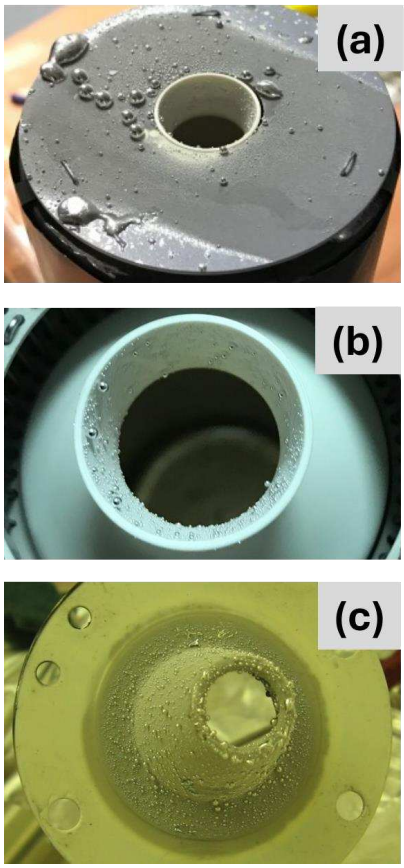


Fig. 4. Representative post-operation morphologies of Ga-source orifice regions observed during routine MBE maintenance after extended high-temperature operation. (a) Open-orifice SUMO-cell source showing Ga rollback traces, elongated droplets, and pooling near the nozzle lip. (b) Enlarged view showing circumferential Ga accumulation and wetting near the aperture, including the inner wall. (c) Insert-based source showing Ga wetting and accumulation around the aperture and across the underside of the insert. The Ga cells used for L1905 and L1907 had a similar insert-based geometry but were of a different model from that shown in (c), and these observations were not temporally linked to those growths.

To examine whether the observed phase behavior is specific to the complex THz QCL multilayer architecture, a thick GaAs reference structure grown in a separate campaign was also analyzed. As shown in Fig. 3(b), this structure exhibits a clear phase departure, with a pronounced change developing late in the growth. The observation of non-monotonic phase behavior in this structurally simple GaAs layer shows that such transient dynamics are not confined to the repeated QCL active-region architecture.

Because the GaAs growth rate under the conditions used here is governed primarily by the Ga flux, available post-operation observations of Ga-source components were examined. Fig. 4 shows representative post-operation morphologies from two different Ga-source configurations. In the open-orifice SUMO-cell geometry, macroscopic rollback traces extend along the surfaces adjacent to the orifice toward the evaporation aperture. Circumferential Ga accumulation and wetting are also visible near the nozzle tip [Figs. 4(a) and 4(b)]. In the insert-based geometry, pronounced Ga accumulation occurs around the aperture perimeter, together with large-area wetting on the underside of the insert [Fig. 4(c)]. The Ga cells used for L1905 and L1907 had a similar insert-based geometry but were of a different model from that shown in Fig. 4(c). These images show substantial liquid-Ga accumulation around the evaporation aperture after extended operation, together with wetting patterns consistent with redistribution. If such redistribution occurs intermittently, it could alter the effective evaporation geometry and produce discrete perturbations in the emitted Ga flux, distinct from smoother source-depletion drift.

High-temperature degassing of the source tip provides a practical means of reducing Ga accumulation, particularly in insert-based sources. In practice, such treatment was often followed by fewer pronounced phase-departure events in subsequent QCL growths. However, this observation is based on repeated operational experience and was not quantified through a controlled before-and-after comparison.

The pyrometry phase depends on optical thickness and can therefore be influenced by growth-rate variation and changes in the material refractive indices. At a given wavelength, the refractive indices depend primarily on temperature, alloy composition, and doping. For the THz QCLs studied here, the average active-region doping concentration is on the order of 10^{15} cm^{-3}, so doping variation is unlikely to produce an appreciable change in the refractive indices. In this study, the substrate temperature was maintained at a constant thermocouple setpoint under PID control, making an abrupt temperature-induced change in the refractive indices unlikely. Within the QCL multilayer, an additional composition-related contribution could arise from variation in the Al flux. However, the thick-GaAs reference exhibits a similar phase departure during an extended undoped GaAs-only growth interval, showing that neither Al deposition nor active-region doping is required for this behavior. Although an Al-related contribution during QCL growth cannot be excluded, previous calibration measurements under comparable conditions showed that long-term changes in the effective QCL growth rate were dominated by changes in the GaAs growth rate [15].

In principle, an apparent phase departure arising solely from changes in the refractive indices would not account for the resolved HRXRD satellite splitting and the corresponding multiple effective periodicities retained in L1905. Among the mechanisms considered here, the combined observations are most consistent with a Ga-related contribution to the observed growth-rate variation, although other mechanisms may also contribute.

5. Device performance and structural periodicity

Fig. 5 compares representative pulsed light–current–voltage (LIV) characteristics of 100 μm × 2 mm single-plasmon THz QCL devices fabricated from L1905 and L1907. For these representative devices, L1907 exhibits a higher peak output power (P_{peak}), a larger operating current-density range (ΔJ), and a higher T_{max}, whereas L1905 shows a more rapid degradation of lasing with increasing temperature.

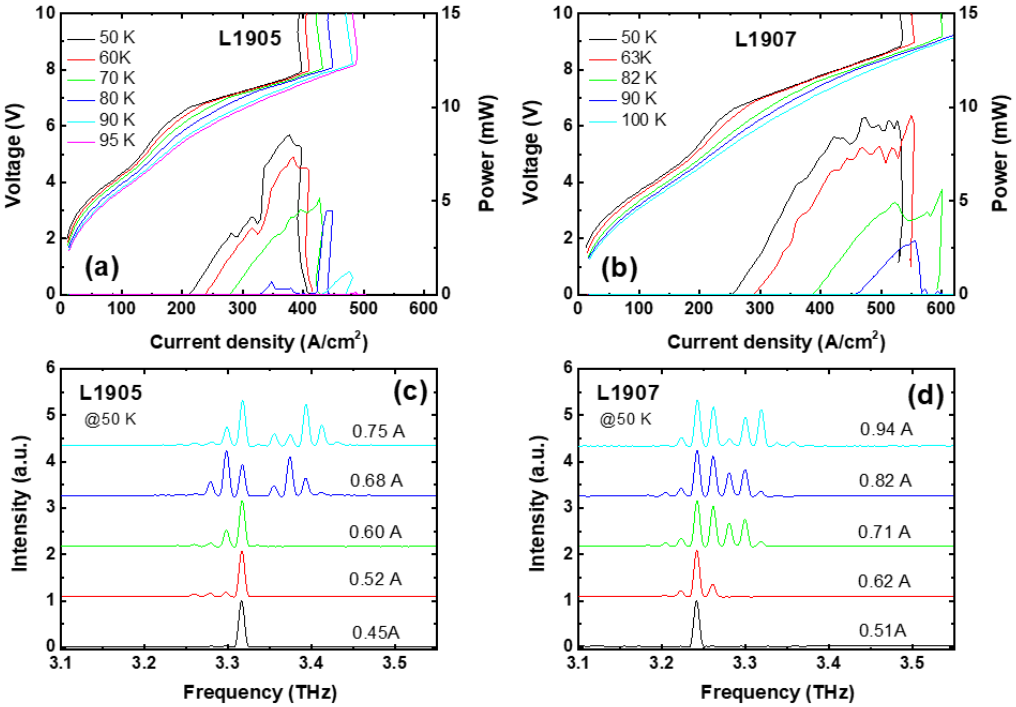


Fig. 5. Pulsed LIV characteristics of 100 μm × 2 mm THz QCLs from (a) L1905 and (b) L1907 at different heat-sink temperatures, and emission spectra at 50 K for (c) L1905 and (d) L1907 at selected drive currents.

A notable feature of the comparison is that L1905 exhibits both a lower threshold current density (J_{th}) and a lower maximum operating current density (J_{max}). At 50 K, L1905 exhibits $J_{th} \approx 213.8$ A cm^{-2} and $J_{max} \approx 376.7$ A cm^{-2}, whereas the corresponding values for L1907 are approximately 254.0 and 525.0 A cm^{-2}, respectively. The lower J_{th} of L1905 therefore does not translate into an extended operating range; instead, its substantially lower J_{max} limits the available operating current-density range.

The voltage characteristics help narrow the interpretation of this difference. L1905 and L1907 exhibit nearly identical turn-on voltages, whereas the maximum operating voltage of L1905 is clearly lower than that of L1907. The similar turn-on voltages suggest that the marked difference between the two devices is unlikely to originate primarily from a generic low-bias injection barrier. The reduced maximum operating voltage of L1905 is instead consistent with a transport limitation that becomes important at higher bias. However, the present measurements do not by themselves determine the microscopic alignment sequence responsible for this behavior.

To assess whether the device-performance differences shown in Fig. 5 were specific to the representative device pair, the comparison was extended to devices with matched ridge widths and cavity lengths. The compared devices were fabricated from near-central regions of the respective wafers. L1905 and L1907 were processed sequentially within the same fabrication batch using the same fabrication procedure. For each matched geometry, devices from the two wafers were mounted on the same copper submount and measured sequentially using the same calibrated THz measurement system. The resulting characteristics from six matched-device comparisons, including the pair shown in Fig. 5 and comprising twelve devices in total, are summarized in Table I. Temperature-dependent LIV characteristics for the 150 μm × 2 mm and 150 μm × 2.5 mm matched-device comparisons listed in Table I are also provided in the Supplementary Material.

Across the six matched comparisons, J_{th} is higher for L1907 in five cases, by approximately 19–35%, with one comparison showing the opposite trend. In contrast, J_{max}, ΔJ, maximum operating temperature, and peak output power are higher for L1907 in all six comparisons. The two wafers share the same nominal doping profile, and the matched devices were processed in the same fabrication batch using the same contact scheme; growth-to-growth variation in the realized doping level cannot, however, be

independently excluded. Thus, although J_{th} does not vary in the same direction in every matched comparison, the higher J_{max}, larger ΔJ, higher T_{max}, and higher P_{peak} of L1907 are reproduced across all six matched comparisons.

Table I. Matched-device characteristics of L1905 and L1907 cleaved-facet single-plasmon THz QCLs. Each pair has the same ridge width and cavity length. $\Delta J = J_{max} - J_{th}$ and was calculated before rounding. Current densities and peak powers were measured at 50 K; T_{max} was determined from temperature-dependent measurements under the same pulsed conditions described in Section 2.

Device dimensions	Wafer	J_{th} (A cm^{-2})	J_{max} (A cm^{-2})	ΔJ (A cm^{-2})	T_{max} (K)	P_{peak} (mW)
100 µm × 1 mm	L1905	392.5	737.5	345.0	76	1.60
	L1907	481.1	1006.0	524.9	98	2.63
100 µm × 1.5 mm	L1905	261.3	394.7	133.3	81	2.76
	L1907	342.7	527.3	184.7	87	4.28
100 µm × 2 mm (pair 1)	L1905	213.8	376.7	162.9	95	8.54
	L1907	254.0	525.0	271.0	100	9.30
100 µm × 2 mm (pair 2)	L1905	280.0	453.0	173.0	93	7.45
	L1907	255.0	545.0	290.0	105	17.9
150 µm × 2 mm	L1905	184.7	364.3	179.7	101	17.6
	L1907	234.7	536.7	302.0	107	23.0
150 µm × 2.5 mm	L1905	150.1	288.0	137.9	98	18.8
	L1907	203.2	432.0	228.8	105	24.2

The HRXRD measurements provide the structural basis for interpreting the device behavior. As discussed in Section 3, L1905 exhibits resolved high-order satellite splitting, indicating multiple effective periodicities within the active region, whereas L1907 retains a single dominant periodicity. A QCL active region comprises repeated cascade periods connected in series and therefore carrying the same current density, so device operation requires a self-consistent field distribution that supports transport throughout the cascade. In a structurally uniform cascade, successive periods share the same nominal layer sequence and are expected to operate under closely matched field-dependent transport conditions; multiple effective periodicities break this uniformity, causing different portions of the active region to reach favorable resonant-alignment conditions at different electric fields. A related common-window constraint has been demonstrated in heterogeneous THz QCLs, where sections with different J_{th} and J_{max} values restrict the overall operating range to their common current-density interval [5]. Here, although the periodicity differences arise from growth rather than deliberate design, the resulting sections can similarly reduce the bias range over which a large fraction of the active region remains favorably aligned, thereby narrowing the common transport window.

Fig. 6 schematically summarizes this physical picture, which may help explain the lower J_{max}, smaller ΔJ, and reduced output power of L1905. Its lower maximum operating voltage and more rapid degradation with increasing temperature are likewise consistent with a high-field transport limitation, although the present measurements do not distinguish transport bottlenecking from possible leakage contributions.

The generally lower J_{th} of L1905, observed in five of the six matched comparisons, requires more cautious interpretation. It does not translate into a larger operating range and should not be taken as evidence of enhanced gain or improved epitaxial quality. The present measurements do not identify its microscopic origin, and no unique mechanism for the lower J_{th} is assigned here.

The average structural and spectral characteristics provide additional, but secondary, information. The unsplit low-order HRXRD satellites yield average effective superlattice periods of approximately 124.6 nm for L1905 and 126.0 nm for L1907, corresponding to deviations of approximately −0.4% and +0.7% from the nominal design value of 125.1 nm. The slightly higher emission frequency of L1905 is qualitatively consistent with its smaller average period. However, the multiple effective periodicities revealed by the high-order satellites preclude interpreting L1905 as a uniformly thinner active region. Its broader multimode spectrum may be compatible with a broader distribution of alignment conditions, but

spectral shape also depends on cavity geometry, facet conditions, current injection, and thermal effects and is therefore not used as primary evidence for structural nonuniformity.

Nevertheless, the primary HRXRD and matched-device measurements show that the retained effective-periodicity differences are accompanied by consistent differences in high-field device performance.

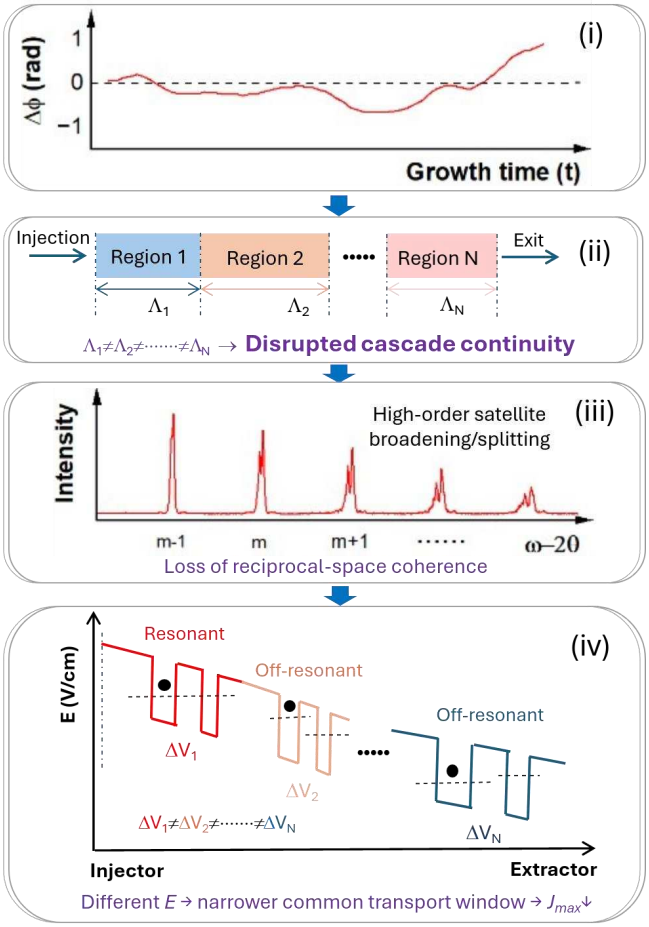


Fig. 6. Schematic illustration of how transient epitaxial dynamics can disrupt cascade continuity. (i) A discrete growth-state change alters the phase evolution relative to the constant-growth-rate reference. (ii) This can partition the active region into portions with different effective periodicities ($\Lambda_1 \neq \Lambda_2 \neq \cdots \neq \Lambda_n$), disrupting cascade continuity. (iii) The retained modulation can reduce long-range reciprocal-space coherence and broaden or split high-order HRXRD satellites. (iv) Series-connected portions may require different field-dependent alignment conditions at the same current, potentially narrowing the common transport window and reducing *Jmax* and the operating range.

6. Conclusion

In conclusion, we have investigated transient growth dynamics in long-duration GaAs/AlGaAs THz QCL heterostructures using in-situ pyrometry, HRXRD, device characterization, and post-operation source observations. The two nominally identical structures exhibit markedly different growth dynamics, distinct effective periodicities, and consistent differences in high-field performance across matched devices. The results support a physical picture in which discrete growth-state changes can disrupt cascade continuity. The combined observations further suggest a Ga-related contribution to the observed transient growth-rate variation, although other mechanisms cannot be excluded. Transient growth dynamics should therefore be considered alongside growth-rate drift, layer thickness, alloy composition, and doping when assessing reproducibility in long-duration THz QCL epitaxy.

Supplementary Material

See the supplementary material for details of the pyrometry analysis, quantitative analysis of the split HRXRD satellite peaks, an HRXRD reference for extended growth, and additional temperature-dependent device-performance measurements.

Acknowledgments

This work was supported by UK Research and Innovation through the Programme Grant TeraCom (EP/W028921/1) and the State Administration of Foreign Experts Affairs, No. D20250184.

Author Contributions

Lianhe Li: Conceptualization, Methodology, Investigation, Writing – original draft. Sumona Kumar: Investigation, Data curation. Thomas Moorhouse: Device fabrication. Minghui You: Methodology. A. Giles Davies: Supervision, Funding acquisition, Writing – review & editing. Edmund H. Linfield: Supervision, Funding acquisition.

Data Availability Statement

The data that support the findings of this study are available from the corresponding author upon reasonable request.

Conflicts of Interest

The authors have no conflicts to disclose.

References

[1] F. R. Giorgetta, P. Gaal, E. Castro-Camus, D. M. Mittleman, M. B. Johnston, K. L. Vodopyanov, K. A. Nelson, P. U. Jepsen, and R. Huber, *The 2023 terahertz science and technology roadmap*, J. Phys. D: Appl. Phys. **56**, 223001 (2023).

[2] M. S. Vitiello and P. De Natale, *Terahertz quantum cascade lasers as enabling quantum technology*, Adv. Quantum Technol. **5**, 2100082 (2022).

[3] R. Köhler, A. Tredicucci, F. Beltram, H. E. Beere, E. H. Linfield, A. G. Davies, D. A. Ritchie, R. C. Iotti, and F. Rossi, "Terahertz semiconductor-heterostructure laser," Nature 417, 156–158 (2002).

[4] D. Turčinková, G. Scalari, F. Castellano, M. I. Amanti, M. Beck and J. Faist, "Ultra-broadband heterogeneous quantum cascade laser emitting from 2.2 to 3.2 THz," Appl. Phys. Lett. **99**, 191104 (2011).

[5] Li, L. H., Garrasi, K., Kundu, I., Han, Y. J., Salih, M., Vitiello, M. S., Davies, A. G., and Linfield, E. H., "Broadband heterogeneous terahertz frequency quantum cascade laser," *Electronics Letters* 54(18), 1089–1091 (2018).

[6] M. Brandstetter, C. Deutsch, M. Krall, et al., "High power terahertz quantum cascade lasers with symmetric wafer bonded active regions", Appl. Phys. Lett., 103, 171113 (2013).

[7] L. H. Li, L. Chen, J. R. Freeman, M. Salih, P. Dean, A. G. Davies, and E. H. Linfield, "Multi-watt high power terahertz frequency quantum cascade lasers," Electron. Lett. 53, 799–800 (2017).

[8] W. Li, Y. Li, Y. Ma, et al., "Continuous-wave terahertz quantum cascade laser based on a hybrid bound to bound quantum design", Front. Photonics 3:1071879 (2022).

[9] S. Fathololoumi, E. Dupont, C. W. I. Chan, Z. R. Wasilewski, S. R. Laframboise, D. Ban, A. Mátyás, C. Jirauschek, Q. Hu, and H. C. Liu, "Terahertz quantum cascade lasers operating up to ~200 K with optimized oscillator strength and improved injection tunneling," Opt. Express 20, 3866–3876 (2012).

[10] A. Khalatpour, A. K. Paulsen, C. Deimert, Z. R. Wasilewski, and Q. Hu, "High-power portable terahertz laser systems," Nat. Photonics 15, 16–20 (2021).

[11] A. Khalatpour, M. C. Tam, S. J. Addamane, J. L. Reno, Z. R. Wasilewski, and Q. Hu, "Enhanced operating temperature in terahertz quantum cascade lasers based on direct phonon depopulation," Appl. Phys. Lett. 122, 161101 (2023).

[12] H. E. Beere, J. C. Fowler, J. Alton, E. H. Linfield, D. A. Ritchie, R. Köhler, A. Tredicucci, G. Scalari, L. Ajili, J. Faist, and S. Barbieri, "MBE growth of terahertz quantum cascade lasers," J. Cryst. Growth 278, 756–764 (2005).

[13] T. Roch, A. M. Andrews, G. Fasching, A. Benz, W. Schrenk, K. Unterrainer, and G. Strasser, "High-quality MBE growth of AlχGa1-χAs-based THz quantum cascade lasers," Cent. Eur. J. Phys. 5, 244–251 (2007).

[14] Z. R. Wasilewski, "MBE growth of THz quantum cascade lasers," in Molecular Beam Epitaxy: From Research to Mass Production, M. Henini, ed. (Elsevier Inc., 2013), Chap. 28.

[15] L. H. Li, J. X. Zhu, L. Chen, A. G. Davies, and E. H. Linfield, "The MBE growth and optimization of high performance terahertz frequency quantum cascade lasers," Opt. Express 23, 2720–2729 (2015).

[16] W. G. Breiland and K. P. Killeen, "A virtual interface method for extracting growth rates and high temperature optical constants from thin semiconductor films using in situ normal incidence reflectance," J. Appl. Phys. 78, 6726–6736 (1995).

[17] S. Barbieri, J. Alton, H. E. Beere, J. Fowler, E. H. Linfield, and D. A. Ritchie, "Quantum cascade lasers operating up to ~70 K in continuous wave," Appl. Phys. Lett. 85, 1674–1676 (2004).

[18] V. S. Speriosu and T. Vreeland Jr., "X-ray rocking curve analysis of superlattices," J. Appl. Phys. 56, 1591–1600 (1984).